Title

Nonlinear edge preserving smoothing and segmentation of 4-D medical images via scale-space fingerprint analysis

Author

Reutter, Bryan W.

Publication Date

2000-11-01

Nonlinear Edge Preserving Smoothing and Segmentation of 4-D Medical Images Via Scale-Space Fingerprint Analysis[1]

Bryan W. Reutter,[†‡] V. Ralph Algazi,[‡] and Ronald H. Huesman[†]

[†]Center for Functional Imaging, Lawrence Berkeley National Laboratory

University of California, Berkeley, California 94720, USA

[‡]Center for Image Processing and Integrated Computing

University of California, Davis, California 95616, USA

Technical Report LBNL-47034

Lawrence Berkeley National Laboratory

November 1, 2000

[1]This work was supported by US Department of Health and Human Services grant P01-HL25840, by US Department of Energy contract DE-AC03-76SF00098, and by the University of California MICRO program. This work was developed in part using the resources at the US Department of Energy National Energy Research Scientific Computing (NERSC) Center.

Abstract

Nonlinear edge preserving smoothing often is performed prior to medical image segmentation. The goal of the nonlinear smoothing is to improve the accuracy of the segmentation by preserving changes in image intensity at the boundaries of structures of interest, while smoothing random fluctuations due to noise in the interiors of the structures. Methods include median filtering and morphology operations such as gray scale erosion and dilation, as well as spatially varying smoothing driven by local contrast measures.

Rather than irreversibly altering the image data prior to segmentation, the approach described here has the potential to unify nonlinear edge preserving smoothing with segmentation based on differential edge detection at multiple scales. The analysis of n-D image data is decomposed into independent 1-D problems that can be solved relatively quickly. Smoothing in various directions along 1-D profiles through n-D data is driven by a measure of local structure separation, rather than by a local contrast measure. Isolated edges are preserved independent of their contrast, given an adequate contrast to noise ratio. In addition, analytic expressions are obtained for the derivatives of the edge preserved 1-D profiles. Using these expressions, multidimensional edge detection operators such as the Laplacian or the second derivative in the direction of the image intensity gradient can be composed and used to segment n-D data. The smoothing and segmentation algorithms are applied to simulated 4-D medical image data.

1 Introduction

Nonlinear edge preserving smoothing often is performed prior to medical image segmentation. The goal of the nonlinear smoothing is to improve the accuracy of the segmentation by preserving changes in image intensity at the boundaries of structures of interest, while smoothing random fluctuations due to noise in the interiors of the structures. Methods include median filtering and morphology operations such as gray scale erosion and dilation [1], as well as spatially varying smoothing driven by local contrast measures [2, 3]. By comparison, linear smoothing via spatially invariant convolution uniformly blurs structure boundaries, as well as noise. The benefits of noise reduction can be offset by deformations of the boundaries that adversely affect the accuracy of the subsequent segmentation.

Rather than irreversibly altering the image data prior to segmentation, the approach described here has the potential to unify nonlinear edge preserving smoothing with segmentation based on differential edge detection at multiple scales. The analysis of multidimensional (n-D) image data is decomposed into independent 1-D problems that can be solved relatively quickly. The elementary 1-D smoothing algorithm is described in Section 2 and is generalized to arbitrary dimension in Section 3. Smoothing in various directions along 1-D profiles through n-D data is driven by a measure of local structure separation, rather than by a local contrast measure. Isolated edges are preserved independent of their contrast, given an adequate contrast to noise ratio (CNR).

In addition, analytic expressions are obtained for the derivatives of the edge preserved 1-D profiles. Using these expressions and the methods described in Section 3, multidimensional edge detection operators such as the Laplacian or the second derivative in the direction of the image intensity gradient can be composed and used to segment n-D data. Computer simulations are used in Section 4 to evaluate the performance of the 1-D smoothing algorithm and 4-D versions of the n-D smoothing and segmentation algorithms. Preliminary results of a 3-D version of the n-D smoothing algorithm were presented in the conference report [4].

Potential applications of these methods include 4-D spatiotemporal segmentation of res-

piratory gated cardiac positron emission tomography (PET) transmission images to improve the accuracy of attenuation correction [5, 6], and 4-D spatiotemporal segmentation of dynamic cardiac single photon emission computed tomography (SPECT) images to facilitate unbiased estimation of time activity curves and kinetic parameters for left ventricular volumes of interest [7].

2 The 1-D Smoothing Algorithm

2.1 Recursive Multiscale Blending

Given linearly smoothed versions of a 1-D signal $\mathrm{f}(x)$ and its first two derivatives at J scales, one can perform nonlinear edge preserving smoothing as follows. The linearly smoothed versions of $\mathrm{f}(x)$ are denoted by $\bar{\mathrm{f}}(x, a_j)$, and the linearly smoothed first and second derivatives are denoted by $\bar{\mathrm{f}}^{(1)}(x, a_j)$ and $\bar{\mathrm{f}}^{(2)}(x, a_j)$, respectively, for $j = 1, \ldots, J$. The scale coordinate a controls the width of the convolution kernels used in the linear filtering. The kernels are based on the uniform cubic B-spline basis function and its first two derivatives [8, 9]. The cubic B-spline has a support of $4a$ and approximates a Gaussian with a standard deviation, σ, of $\sqrt{1/3}\, a$. Dyadic sampling of the scale coordinate a is used, yielding $a_j = 2^{j-1} a_1$.

The nonlinearly smoothed versions of $\mathrm{f}(x)$, denoted by $\tilde{\mathrm{f}}(x, a_j)$, are obtained by recursively blending the linearly smoothed versions:

$$\tilde{\mathrm{f}}(x, a_j) = \begin{cases} \bar{\mathrm{f}}(x, a_1) & j = 1 \\ [1 - \mathrm{C}_j(x)]\, \tilde{\mathrm{f}}(x, a_{j-1}) + \mathrm{C}_j(x) \bar{\mathrm{f}}(x, a_j) & j = 2, \ldots, J. \end{cases} \tag{1}$$

The blending functions $\{\mathrm{C}_j(x);\, j = 2, \ldots, J\}$ play a role similar to that of the spatially varying diffusion coefficients used in typical implementations of edge preserving smoothing via inhomogeneous diffusion (e.g., [2]). When $\mathrm{C}_j(x_0) = 0$, smoothing stops in the neighborhood of x_0 and $\tilde{\mathrm{f}}(x_0, a_j)$ remains unchanged from the value $\tilde{\mathrm{f}}(x_0, a_{j-1})$ obtained using nonlinear smoothing at the previous, finer scale. When $\mathrm{C}_j(x_0) = 1$, smoothing is unabated and $\tilde{\mathrm{f}}(x_0, a_j)$

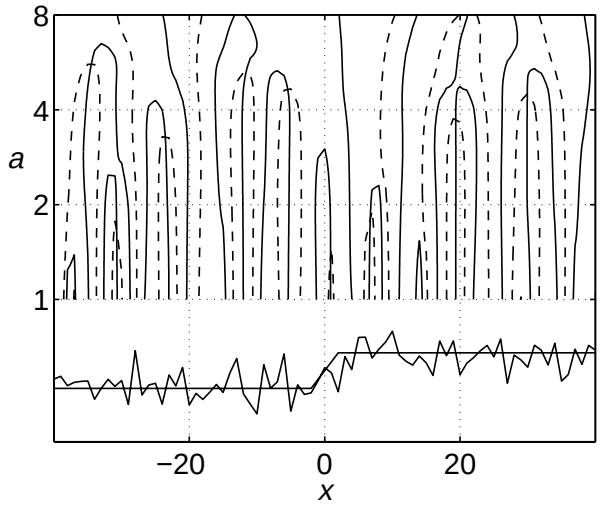

Figure 1: Augmented scale-space fingerprint for an isolated edge of width four and a CNR of 2.5. Solid fingerprint lines depict the zero-crossing locations of $\bar{\mathrm{f}}^{(2)}(x, a)$ (i.e., edge and ledge locations) over a continuum of scales. Dashed lines depict the zero-crossing locations of $\bar{\mathrm{f}}^{(1)}(x, a)$ (i.e., ridge and trough locations). The noiseless signal is shown with the noisy signal below the fingerprint.

is set to the value $\bar{\mathrm{f}}(x_0, a_j)$ obtained using linear smoothing at the current, coarser scale.

2.2 Defining the Multiscale Blending Functions

The multiscale blending functions $\{\mathrm{C}_j(x);\, j = 2, \ldots, J\}$ are defined via the following analysis of the augmented scale-space fingerprint for $\mathrm{f}(x)$. The augmented scale-space fingerprint (Figure 1) is a graphical depiction of the locations of the zero-crossings of the first two derivatives of the linearly smoothed signal as a function of scale [9]. At a particular scale a_j, each zero-crossing location of $\bar{\mathrm{f}}^{(2)}(x, a_j)$ is labeled as either a local maximum (edge) or local minimum (ledge) in gradient magnitude, depending on its proximity to nearby zero-crossing locations of $\bar{\mathrm{f}}^{(1)}(x, a_j)$ (i.e., ridges and troughs). For each of the resulting edge locations $\{x_{jk};\, k = 1, \ldots, K_j\}$, the distance Δx_{jk} separating the ridge, trough, or ledge on either side of the edge is calculated. The blending function $\mathrm{C}_j(x)$ is then assigned values ranging between zero and one at the edge locations, based on the separation distances $\{\Delta x_{jk};\, k = 1, \ldots, K_j\}$.

The value assigned to $\mathrm{C}_j(x)$ at the edge location x_{jk} is denoted by γ_{jk} and is selected using a monotonically decreasing function that maps larger separation distances to smaller values. This heuristic mapping is based on the observation that the separation distance Δx tends to be larger for an isolated true edge, than it is for a random second derivative zero-crossing

associated with noise (Figure 1). For simplicity, a piecewise linear mapping is used:

$$\gamma_{jk} = \begin{cases} 1 & \Delta x_{jk} < \alpha_j \\ 1 - \frac{\Delta x_{jk} - \alpha_j}{\beta_j - \alpha_j} & \alpha_j \le \Delta x_{jk} < \beta_j \\ 0 & \beta_j \le \Delta x_{jk}, \end{cases} \tag{2}$$

where α_j and β_j are selected as follows. The separation distances $\{\Delta x_{jk};\, k = 1, \ldots, K_j\}$ are first sorted in ascending order, and then α_j and β_j are set to values corresponding to a lower and an upper percentile of the sorted values, respectively. The lower and upper percentiles can be selected based on the expected numbers of true and random edges at the j^{th} scale. In practice, the expected number of random edges due to noise in the linearly smoothed signal $\bar{\mathrm{f}}(x, a_j)$ will vary roughly inversely with the scale a_j, while the number of isolated true edges will remain roughly constant.

Given the values $\{\gamma_{jk};\, k = 1, \ldots, K_j\}$ at the edge locations, the blending function $\mathrm{C}_j(x)$ can be defined for all x as follows. The blending function $\mathrm{C}_j(x)$ must be continuous through at least its second derivative, in order for the nonlinearly smoothed signal $\tilde{\mathrm{f}}(x, a_j)$ to have continuous first and second derivatives. Rearranging the factors in equation (1) and denoting the first and second derivatives of $\mathrm{C}_j(x)$ by $\mathrm{C}_j^{(1)}(x)$ and $\mathrm{C}_j^{(2)}(x)$, respectively, one obtains the following expressions for the first and second derivatives of the nonlinearly smoothed signal $\tilde{\mathrm{f}}(x, a_j)$:

$$\tilde{\mathrm{f}}^{(1)}(x, a_j) = \begin{cases} \bar{\mathrm{f}}^{(1)}(x, a_1) & j = 1 \\ \tilde{\mathrm{f}}^{(1)}(x, a_{j-1}) + \mathrm{C}_j(x) \left[\bar{\mathrm{f}}^{(1)}(x, a_j) - \tilde{\mathrm{f}}^{(1)}(x, a_{j-1})\right] & \\ \qquad + \mathrm{C}_j^{(1)}(x) \left[\bar{\mathrm{f}}(x, a_j) - \tilde{\mathrm{f}}(x, a_{j-1})\right] & j = 2, \ldots, J \end{cases} \tag{3}$$

$$\tilde{\mathrm{f}}^{(2)}(x, a_j) = \begin{cases} \bar{\mathrm{f}}^{(2)}(x, a_1) & j = 1 \\ \tilde{\mathrm{f}}^{(2)}(x, a_{j-1}) + \mathrm{C}_j(x) \left[\bar{\mathrm{f}}^{(2)}(x, a_j) - \tilde{\mathrm{f}}^{(2)}(x, a_{j-1})\right] & \\ \qquad + 2\mathrm{C}_j^{(1)}(x) \left[\bar{\mathrm{f}}^{(1)}(x, a_j) - \tilde{\mathrm{f}}^{(1)}(x, a_{j-1})\right] & j = 2, \ldots, J. \\ \qquad + \mathrm{C}_j^{(2)}(x) \left[\bar{\mathrm{f}}(x, a_j) - \tilde{\mathrm{f}}(x, a_{j-1})\right] & \end{cases} \tag{4}$$

To achieve the desired continuity in a relatively straightforward fashion, the blending function $\mathrm{C}_j(x)$ is defined to be the piecewise quartic function

$$\mathrm{C}_j(x) = \begin{cases} \gamma_{j1} & x < x_{j1} \\ \gamma_{j(k-1)} + \left[\gamma_{jk} - \gamma_{j(k-1)}\right] \mathrm{S}_{jk}(x) & x_{j(k-1)} \le x < x_{jk}; k = 2, \ldots, K_j \\ \gamma_{jK_j} & x_{jK_j} \le x, \end{cases} \tag{5}$$

where $\mathrm{S}_{jk}(x)$ is a smooth step function obtained by integrating the uniform cubic B-spline basis function on which the linear smoothing is based:

$$\mathrm{S}_{jk}(x) = \int_{x_{j(k-1)}}^{x} \frac{1}{v_{jk}} \Pi^{*4}\left(\frac{u - u_{jk}}{v_{jk}}\right) du, \tag{6}$$

where $u_{jk} = \left[x_{j(k-1)} + x_{jk}\right]/2$, $v_{jk} = \left[x_{jk} - x_{j(k-1)}\right]/4$, and $\Pi^{*4}(u)$ denotes the uniform cubic B-spline basis function. The function $\mathrm{S}_{jk}(x)$ is zero at $x = x_{j(k-1)}$ and increases monotonically to one at $x = x_{jk}$. It is continuous through its third derivative, and its first through third derivatives are all zero at both $x = x_{j(k-1)}$ and $x = x_{jk}$. Thus, using this construction one obtains a blending function $\mathrm{C}_j(x)$ that ranges between zero and one and is continuous through its third derivative. In Section 4.1, this 1-D smoothing algorithm is applied to a simulated 1-D edge.

3 The n-D Smoothing and Segmentation Algorithms

Edges can be preserved in multidimensional image data by applying the 1-D smoothing algorithm described in Section 2 independently along the coordinate axis directions, as well as along the diagonal directions of the 2-D planes spanned by the coordinate axes, and averaging the results. This builds on the work described in [2], in which processing was performed only along the coordinate axis directions. In Section 4.2, a 4-D version of the smoothing algorithm is applied to simulated respiratory gated PET transmission images.

By processing the diagonal directions, additional information is obtained that allows one to characterize the first and second order differential properties of the data in any direction.

Using this additional information, multidimensional edge detection operators such as the Laplacian or the second derivative in the direction of the image intensity gradient can be composed and used to segment the data as follows.

The n-D data array is denoted by $\mathrm{f}(\mathbf{x})$, where $\mathbf{x} = [x_1 \quad \cdots \quad x_n]^{\mathrm{T}}$ is the position vector for the domain of the data and "$[\,]^{\mathrm{T}}$" denotes the matrix transpose. The 1-D profile passing through the point $\mathbf{x}_0$ in the direction $\mathbf{v}_0$ is denoted by

$$\mathrm{f}_{\mathbf{x}_0,\mathbf{v}_0}(s) = \mathrm{f}(\mathbf{x}_0 + s\mathbf{v}_0), \tag{7}$$

where $\mathbf{v} = [v_1 \quad \cdots \quad v_n]^{\mathrm{T}}$ is a unit vector and s is an arc length parameter.

The relationships between the first and second derivatives along the 1-D profile $\mathrm{f}_{\mathbf{x},\mathbf{v}}(s)$ and the first and second order partial derivatives of the n-D data $\mathrm{f}(\mathbf{x})$ are

$$\frac{d\mathrm{f}_{\mathbf{x},\mathbf{v}}}{ds} = \mathbf{v}\cdot\nabla\mathrm{f} = \begin{bmatrix} v_1 & \cdots & v_n \end{bmatrix} \begin{bmatrix} \frac{\partial \mathrm{f}}{\partial x_1} \\ \vdots \\ \frac{\partial \mathrm{f}}{\partial x_n} \end{bmatrix} = \mathbf{v}^{\mathrm{T}}\mathbf{g} \tag{8}$$

$$\frac{d^2\mathrm{f}_{\mathbf{x},\mathbf{v}}}{ds^2} = \mathbf{v}\cdot\nabla[\mathbf{v}\cdot\nabla\mathrm{f}] = \begin{bmatrix} v_1 & \cdots & v_n \end{bmatrix} \begin{bmatrix} \frac{\partial^2 \mathrm{f}}{\partial {x_1}^2} & \cdots & \frac{\partial^2 \mathrm{f}}{\partial x_1 \partial x_n} \\ \vdots & & \vdots \\ \frac{\partial^2 \mathrm{f}}{\partial x_1 \partial x_n} & \cdots & \frac{\partial^2 \mathrm{f}}{\partial {x_n}^2} \end{bmatrix} \begin{bmatrix} v_1 \\ \vdots \\ v_n \end{bmatrix} = \mathbf{v}^{\mathrm{T}}\mathbf{H}\mathbf{v}, \tag{9}$$

where $\mathbf{g}(\mathbf{x})$ is the gradient vector and the matrix $\mathbf{H}(\mathbf{x})$ of second order partial derivatives is the Hessian matrix. For convenience one can write $\mathbf{v}^{\mathrm{T}}\mathbf{H}\mathbf{v}$ as the inner product $\mathbf{w}^{\mathrm{T}}\mathbf{h}$ of the $(\frac{n^2+n}{2})$-element vectors

$$\mathbf{w} = \begin{bmatrix} v_1^2 & 2v_1v_2 & \cdots & 2v_1v_n & v_2^2 & 2v_2v_3 & \cdots & 2v_2v_n & \cdots & v_{n-1}^2 & 2v_{n-1}v_n & v_n^2 \end{bmatrix}^{\mathrm{T}} \tag{10}$$

$$\mathbf{h}(\mathbf{x}) = \begin{bmatrix} \frac{\partial^2 \mathrm{f}}{\partial {x_1}^2} & \frac{\partial^2 \mathrm{f}}{\partial x_1 \partial x_2} & \cdots & \frac{\partial^2 \mathrm{f}}{\partial x_1 \partial x_n} & \frac{\partial^2 \mathrm{f}}{\partial {x_2}^2} & \frac{\partial^2 \mathrm{f}}{\partial x_2 \partial x_3} & \cdots & \frac{\partial^2 \mathrm{f}}{\partial x_2 \partial x_n} & \cdots & \frac{\partial^2 \mathrm{f}}{\partial {x_{n-1}}^2} & \frac{\partial^2 \mathrm{f}}{\partial x_{n-1} \partial x_n} & \frac{\partial^2 \mathrm{f}}{\partial {x_n}^2} \end{bmatrix}^{\mathrm{T}}. \tag{11}$$

Given first and second derivative estimates from 1-D profile processing along each coordinate axis direction and along the diagonal directions of the 2-D planes spanned by the

coordinate axes (for a total of n^2 directions), one can form least squares estimates of the gradient vector $\mathbf{g}(\mathbf{x})$ and the vector $\mathbf{h}(\mathbf{x})$ of Hessian matrix elements as follows. The n^2 direction vectors for the 1-D profiles and the corresponding $\mathbf{w}$ vectors are stored in the matrices

$$\mathbf{V} = \begin{bmatrix} \mathbf{v}_1^{\mathrm{T}} \\ \vdots \\ \mathbf{v}_{n^2}^{\mathrm{T}} \end{bmatrix} \qquad \mathbf{W} = \begin{bmatrix} \mathbf{w}_1^{\mathrm{T}} \\ \vdots \\ \mathbf{w}_{n^2}^{\mathrm{T}} \end{bmatrix}. \tag{12}$$

The first and second derivative estimates along the 1-D profiles are stored in the vectors

$$\mathbf{f}^{(1)}(\mathbf{x}) = \begin{bmatrix} \frac{d\mathrm{f}_{\mathbf{x},\mathbf{v}_1}}{ds} \\ \vdots \\ \frac{d\mathrm{f}_{\mathbf{x},\mathbf{v}_{n^2}}}{ds} \end{bmatrix} \qquad \mathbf{f}^{(2)}(\mathbf{x}) = \begin{bmatrix} \frac{d^2\mathrm{f}_{\mathbf{x},\mathbf{v}_1}}{ds^2} \\ \vdots \\ \frac{d^2\mathrm{f}_{\mathbf{x},\mathbf{v}_{n^2}}}{ds^2} \end{bmatrix}. \tag{13}$$

The vectors $\hat{\mathbf{g}}(\mathbf{x})$ and $\hat{\mathbf{h}}(\mathbf{x})$ are desired, which minimize the weighted sums of squared errors

$$\chi_1^2 = \left[\mathbf{f}^{(1)} - \mathbf{V}\hat{\mathbf{g}}\right]^{\mathrm{T}} \mathbf{\Psi}_1 \left[\mathbf{f}^{(1)} - \mathbf{V}\hat{\mathbf{g}}\right] \tag{14}$$

$$\chi_2^2 = \left[\mathbf{f}^{(2)} - \mathbf{W}\hat{\mathbf{h}}\right]^{\mathrm{T}} \mathbf{\Psi}_2 \left[\mathbf{f}^{(2)} - \mathbf{W}\hat{\mathbf{h}}\right], \tag{15}$$

where $\mathbf{\Psi}_1(\mathbf{x})$ and $\mathbf{\Psi}_2(\mathbf{x})$ are symmetric weighting matrices. Typically, $\mathbf{\Psi}_1(\mathbf{x})$ and $\mathbf{\Psi}_2(\mathbf{x})$ are either identity matrices for unweighted least squares estimates, or the respective inverses of the covariance matrices for $\mathbf{f}^{(1)}(\mathbf{x})$ and $\mathbf{f}^{(2)}(\mathbf{x})$ for weighted least squares estimates.

The resulting least squares estimates for the gradient vector $\mathbf{g}(\mathbf{x})$ and the vector $\mathbf{h}(\mathbf{x})$ of Hessian matrix elements are

$$\hat{\mathbf{g}}(\mathbf{x}) = \left[\mathbf{V}^{\mathrm{T}}\mathbf{\Psi}_1\mathbf{V}\right]^{-1} \mathbf{V}^{\mathrm{T}}\mathbf{\Psi}_1\mathbf{f}^{(1)} \tag{16}$$

$$\hat{\mathbf{h}}(\mathbf{x}) = \left[\mathbf{W}^{\mathrm{T}}\mathbf{\Psi}_2\mathbf{W}\right]^{-1} \mathbf{W}^{\mathrm{T}}\mathbf{\Psi}_2\mathbf{f}^{(2)}. \tag{17}$$

Using these estimates of the gradient vector and the elements of the Hessian matrix, one can compose multidimensional edge detection operators such as the Laplacian, $\sum_{p=1}^{n} \frac{\partial^2 \mathrm{f}}{\partial {x_p}^2}$, or the second derivative in the direction of the gradient, weighted by the squared magnitude of the gradient, $\sum_{p=1}^{n}\sum_{q=1}^{n} \frac{\partial \mathrm{f}}{\partial x_p}\frac{\partial \mathrm{f}}{\partial x_q}\frac{\partial^2 \mathrm{f}}{\partial x_p \partial x_q}$. In Section 4.3, 4-D Laplacian operators are composed and used to segment simulated respiratory gated PET transmission images.

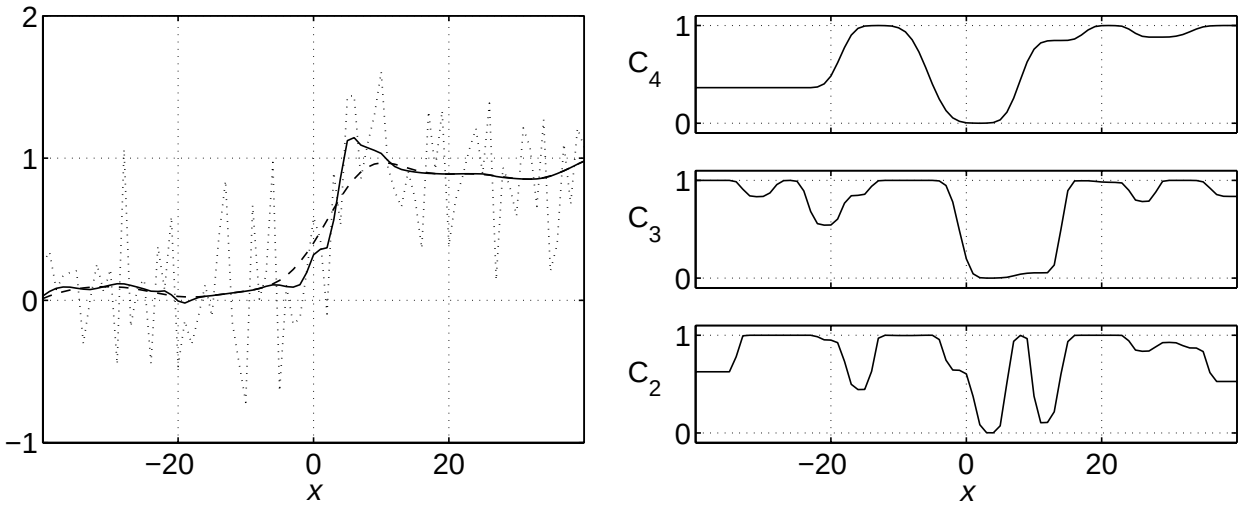

(a) (b)

Figure 2: Results for a simulated 1-D edge of width four and a CNR of 2.5. In (a), the dashed line and the solid line depict the linear and nonlinear smoothing results, respectively, at the scale $a_4 = 8$. The dotted line depicts the unsmoothed signal, which is shown also in Figure 1 with its scale-space fingerprint and the noiseless signal. The blending functions used to perform the nonlinear smoothing are shown in (b).

4 Computer Simulations

4.1 Smoothing a 1-D Edge

To evaluate the performance of the 1-D smoothing algorithm, Gaussian white noise was added to a simulated signal composed of a single ramp transition of width four and a CNR of 2.5 (Figure 1). Linear smoothing was performed at four scales using uniform cubic B-spline basis functions with scale parameters $a_1 = 1$, $a_2 = 2$, $a_3 = 4$, and $a_4 = 8$. Nonlinear smoothing was performed at the scales a_2, a_3, and a_4, using equation (1). Results at the scale a_4 are shown in Figure 2a.

The blending functions $C_2(x)$, $C_3(x)$, and $C_4(x)$ shown in Figure 2b were defined using values for β_2, β_3, and β_4 in equation (2) corresponding to the 94^{th}, 89^{th}, and 80^{th} percentiles of the sorted separation distances, respectively. The upper percentile for β_4 was selected so

that four out of every five edges would undergo some smoothing at the coarsest scale, $a_4 = 8$. Then, using the heuristic that the expected number of random edges due to noise varies roughly inversely with scale, the upper percentiles for β_3 and β_2 were selected so that eight out of nine edges and 16 out of 17 edges would undergo some smoothing at the finer scales $a_3 = 4$ and $a_2 = 2$, respectively. The lower percentiles associated with α_2, α_3, and α_4 in equation (2) were selected to be one-half of the upper percentiles, i.e., the 47^{th}, 44^{th}, and 40^{th} percentiles, respectively.

The nonlinear smoothing yielded a sharper edge than did the linear smoothing, and provided comparable smoothing away from the edge (Figure 2a). Because of the high noise level, the apparent position of the edge was shifted to the right. The blending functions consistently reached their minimum near the edge, thus reducing the amount of smoothing in the neighborhood of the edge (Figure 2b). Away from the edge, the blending functions increased, thus increasing the amount of smoothing.

4.2 Smoothing 4-D Respiratory Gated PET Transmission Images

A 4-D version of the n-D smoothing algorithm was applied to simulated respiratory gated PET transmission images (Figure 3a) generated using the Mathematical Cardiac Torso (MCAT) phantom [10]. The 4-D image array was composed of 40 contiguous 5 mm-thick transverse slices at 15 respiratory phases. Each transverse slice had 80×80 pixels with pixel size 5×5 mm. Diaphragm and heart motion of 15 mm in the superior-inferior direction was simulated, in conjunction with chest wall diameter changes of 9.8 mm in the left-right direction and 20 mm in the anterior-posterior direction. The attenuation coefficients for soft tissue and lung were 0.093 cm^{-1} and 0.027 cm^{-1}, respectively. Gaussian white noise with a standard deviation of 0.019 cm^{-1} was added to the images to yield a CNR of 5 at the air-soft tissue boundary and a CNR of 3.5 at the soft tissue-lung boundaries (Figure 3b).

The 1-D smoothing algorithm was applied independently along the x, y, z, and t spatiotemporal coordinate axis directions of the noisy 80×80×40×15 dataset, using the same

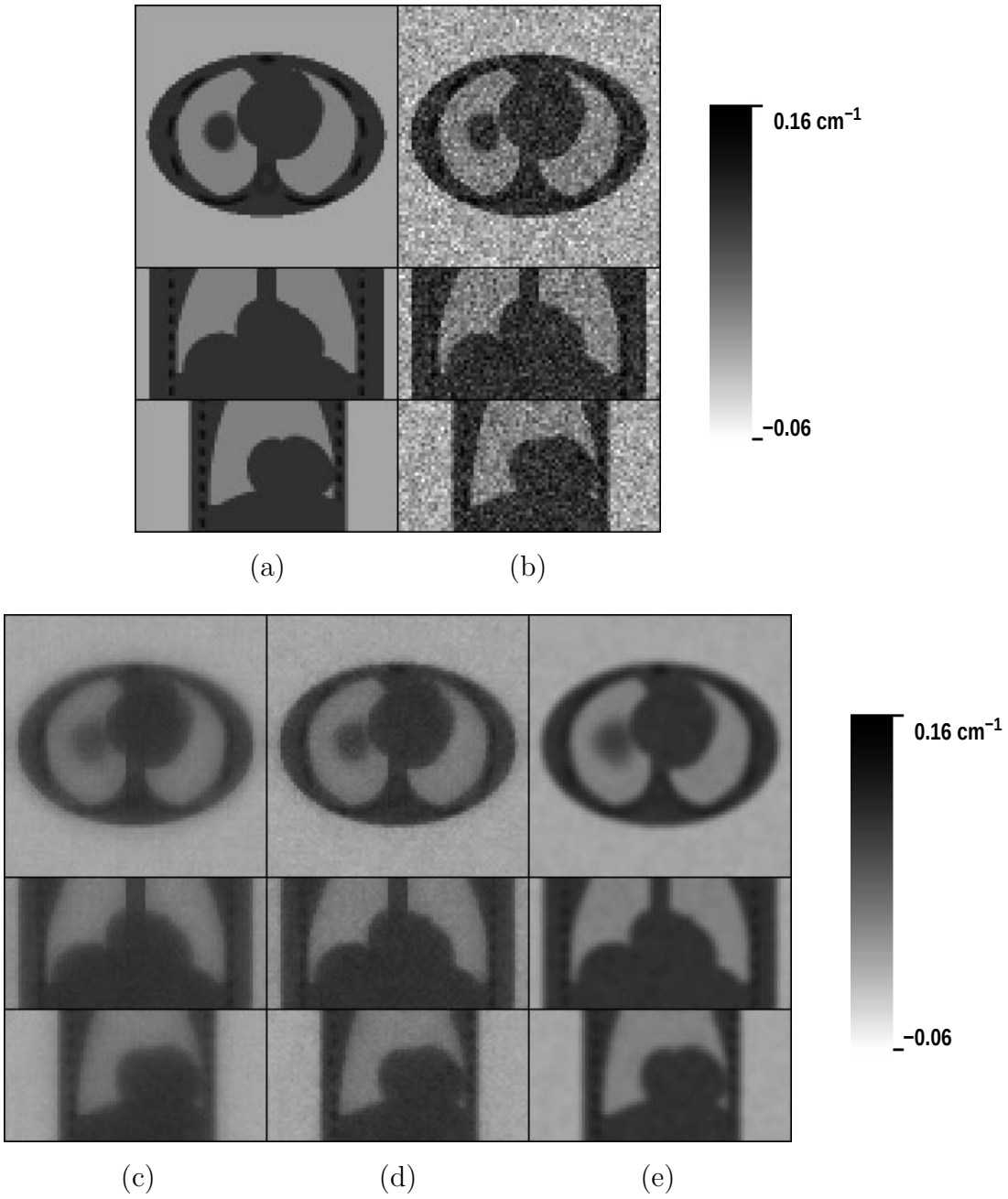

Figure 3: Smoothing results for simulated 4-D respiratory gated PET transmission images. (a) Original noiseless images; (b) original noisy images; (c) average of large scale (1×35) 1-D linear smoothing operators applied along the four coordinate axis directions and twelve diagonal directions; (d) large scale nonlinear smoothing; and (e) 7×7×7×7 linear smoothing. The top, middle, and bottom rows show transverse, coronal, and sagittal cross sections, respectively, through data for respiratory phase 8.

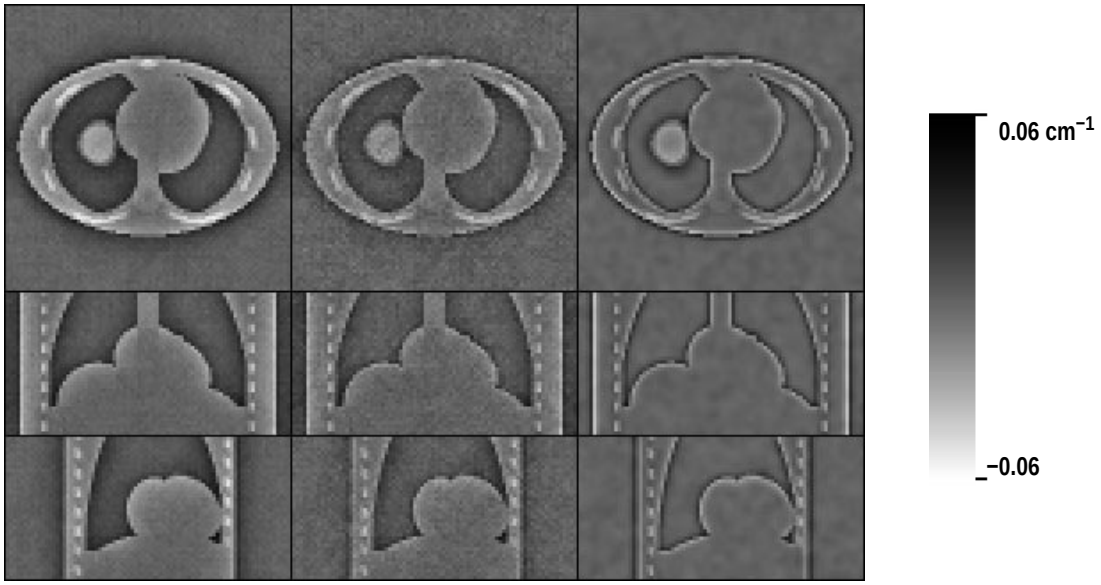

(a) (b) (c)

Figure 4: Differences between (a) Figures 3c and 3a, (b) Figures 3d and 3a, and (c) Figures 3e and 3a.

linear filters that were used to process the simulated 1-D edge in Section 4.1. Six diagonal directions in the xy (transverse), xz (coronal), and yz (sagittal) spatial planes were also processed, along with six diagonal directions in the xt, yt, and zt spatiotemporal planes. Figure 3c shows the results of simply averaging the outputs of the 16 large scale (1×35) 1-D linear filters, corresponding to the scale parameter $a_4 = 8$. This linear smoothing operation was effective at reducing the noise, at the expense of blurring the edges and biasing the attenuation coefficients because of the relatively long support of the 1-D filters. Figure 4a shows the difference between Figure 3c and the noiseless images in Figure 3a. The root mean square (RMS) difference with respect to the noiseless images was reduced to 0.013 cm^{-1}, from the value 0.019 cm^{-1} for the noisy images in Figure 3b.

Figure 3d shows the results of nonlinear smoothing at the scale $a_4 = 8$. The multiscale blending functions $C_2(x)$–$C_4(x)$ were defined using the same values for β_2–β_4 and α_2–α_4 in equation (2), which were used to process the simulated 1-D edge in Section 4.1. Compared to the linear smoothing, this nonlinear smoothing operation was less effective at reducing

the noise, as expected. However, the edges are sharper and there is less bias, as desired. Figure 4b shows the difference between Figure 3d and the noiseless images in Figure 3a. Overall, the RMS difference with respect to the noiseless images improved to 0.0098 cm^{-1}.

For comparison, Figure 3e shows the results of linear smoothing with a 7×7×7×7 separable filter composed from the 1-D filter corresponding to the scale parameter $a_1 = 1$. Compared to the nonlinear smoothing, this separable filtering operation was more effective at reducing the noise, at the expense of adding spatiotemporal correlation to the noise. The edges are also more blurred, but there is less bias in the interiors of the structures. Figure 4c shows the difference between Figure 3e and the noiseless images in Figure 3a. The RMS difference with respect to the noiseless images improved further, to 0.0080 cm^{-1}.

The multidirectional 1-D linear and nonlinear smoothing results shown in Figures 3c and 3d were obtained using an average of 11 minutes of processing for each of the 16 directions, on a 195 MHz MIPS R10000-based Silicon Graphics workstation. The processing of the 16 directions can be done in parallel. Because each individual 1-D profile in each direction can be processed independently, massive parallelization is also possible.

4.3 Segmenting 4-D Respiratory Gated PET Transmission Images

In conjunction with the multidirectional 1-D processing described in Section 4.2, the first and second derivatives of the nonlinearly smoothed 1-D profiles were calculated using equations (3) and (4). Using the methods described in Section 3, 4-D Laplacian edge detection operators were composed and applied to the linearly and nonlinearly processed results shown in Figures 3c and 3d. These 4-D Laplacian calculations took a total of 7 minutes on a 195 MHz MIPS R10000-based Silicon Graphics workstation. In addition, the 4-D Laplacian was calculated for the results of the separable processing shown in Figure 3e.

For respiratory phase 8, 3-D models for the Laplacian zero-crossing surfaces were constructed automatically in less than one minute using the methods described in [5]. Distinct torso and lung surfaces were obtained for each of the three processing methods. The torso

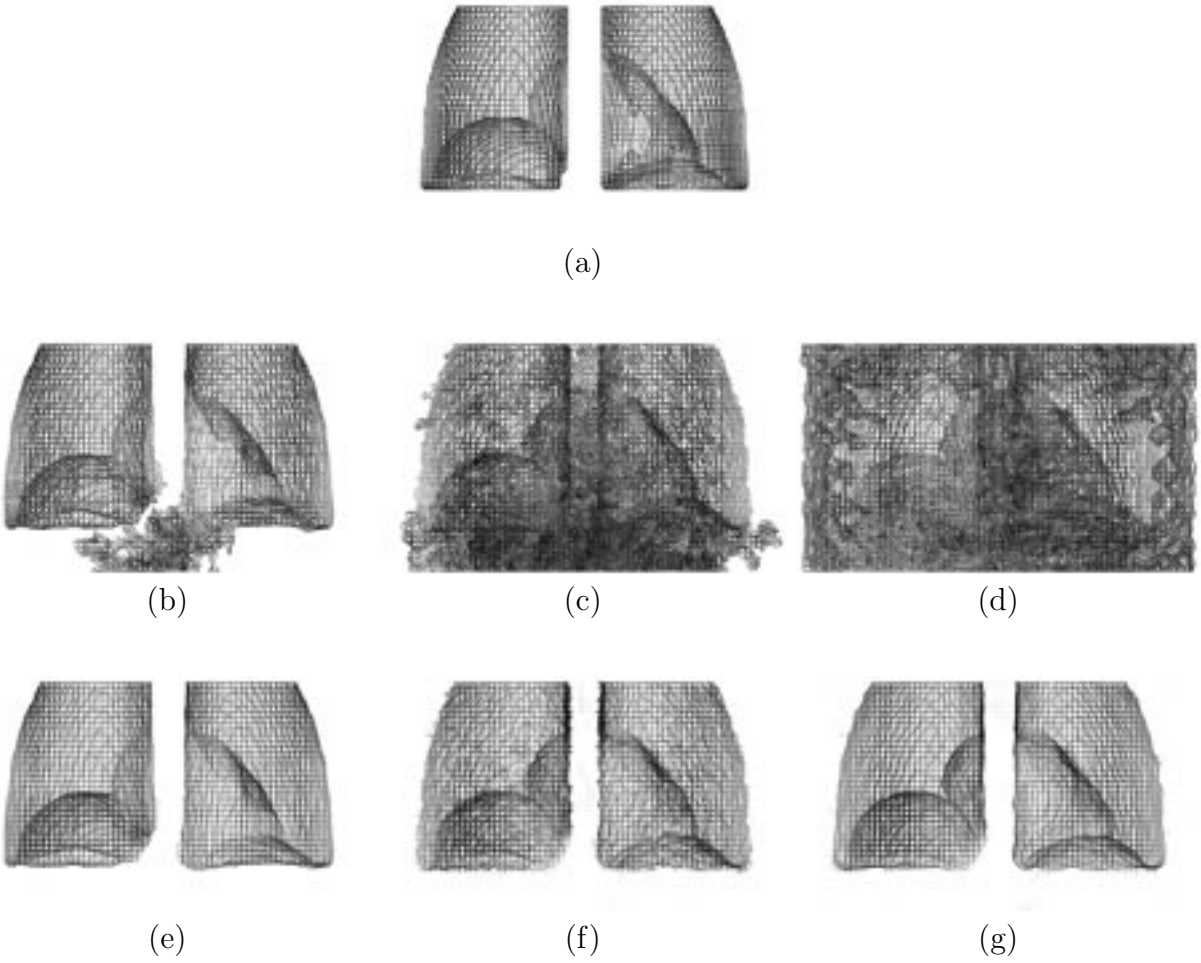

Figure 5: Anterior coronal views of wireframe models for lung surfaces segmented from simulated 4-D respiratory gated PET transmission images. (a) Known lung surfaces extracted from noiseless data shown in Figure 3a; (b, c, d) surfaces extracted from data shown in Figures 3c, 3d, and 3e, respectively; and (e, f, g) use of transparency to show significant portions of surfaces in (b, c, d), respectively.

surfaces agreed well with the known torso surfaces. Anterior coronal views of the wireframe models for the lung surfaces are shown in Figure 5. As a reference, Figure 5a shows the known lung surfaces, which were extracted directly from the noiseless images using a threshold equal to the average of the lung and soft tissue attenuation coefficients.

For the multidirectional 1-D linear processing results shown in Figure 3c, two distinct lung surfaces were obtained (Figure 5b). The segmentation for one lung "leaks" into the

abdomen, but otherwise the lung models agree qualitatively with the known lung surfaces.

For the multidirectional 1-D nonlinear processing results shown in Figure 3d and the separable 4-D processing results shown in Figure 3e, the lungs are joined together and the segmentations leak more extensively (Figures 5c and 5d, respectively).

Figures 5e, 5f, and 5g show the results of modulating the transparencies of the wireframes shown in Figures 5b, 5c, and 5d, respectively, by estimates of the local image intensity gradient magnitude. For each of the three processing methods, the significant portions of the surfaces associated with a relatively large image intensity gradient magnitude are now seen to agree qualitatively with the known lung surfaces.

5 Future Directions

The computer simulations in Section 4 demonstrate that nonlinear edge preserving smoothing and segmentation of 4-D medical images can be performed in a timely manner on a workstation. The simulation results suggest that multidirectional 1-D processing and analysis at multiple spatiotemporal scales can provide rich mathematical and geometric information about possible structures of interest in the images.

Additional work is needed to optimize the multiscale blending functions to balance reductions in variance with increases in bias when processing tomographic image reconstructions. Further study is needed to understand the factors that affect the accuracy of segmentation.

6 Acknowledgment

The authors thank the University of North Carolina Medical Imaging Research Laboratory for making the MCAT phantom available.

This work was supported by the National Heart, Lung, and Blood Institute of the US Department of Health and Human Services under grant P01-HL25840; by the Director, Office of Science, Office of Biological and Environmental Research, Medical Sciences Division of the

US Department of Energy under contract DE-AC03-76SF00098; and by the University of California MICRO program. This work was developed in part using the resources at the US Department of Energy National Energy Research Scientific Computing (NERSC) Center.

References

[1] S R Sternberg. Grayscale morphology. *Comput Vis Graph Imag Process*, 35(3):333–355, 1986.

[2] J Weickert, B M T H Romeny, and M A Viergever. Efficient and reliable scheme for nonlinear diffusion filtering. *IEEE Trans Imag Process*, 7(3):398–410, 1998.

[3] K Kitamura, H Iida, M Shidahara, S Miura, and I Kanno. Noise reduction in PET attenuation correction using non-linear Gaussian filters. *IEEE Trans Nucl Sci*, 47(3):994–999, 2000.

[4] B W Reutter, V R Algazi, and R H Huesman. Computationally efficient nonlinear edge preserving smoothing of n-D medical images via scale-space fingerprint analysis. In M Ulma, editor, *2000 IEEE Nuclear Science Symposium and Medical Imaging Conference Record*, in press.

[5] B W Reutter, G J Klein, and R H Huesman. Automated 3-D segmentation of respiratory-gated PET transmission images. *IEEE Trans Nucl Sci*, 44(6):2473–2476, 1997.

[6] B W Reutter, G J Klein, and R H Huesman. Respiration-compensated cardiac PET attenuation correction via automated 4-D segmentation of gated transmission images. *J Nucl Med*, 38(5 suppl):203P, 1997. (Abstract).

[7] B W Reutter, G T Gullberg, and R H Huesman. Direct least-squares estimation of spatiotemporal distributions from dynamic SPECT projections using a spatial segmentation and temporal B-splines. *IEEE Trans Med Imag*, 19(5):434–450, 2000.

[8] Y-P Wang and S L Lee. Scale-space derived from B-splines. *IEEE Trans Patt Anal Mach Intell*, 20(10):1040–1055, 1998.

[9] B W Reutter and V R Algazi. Computationally efficient anisotropic scale-space processing of 4-D medical images. Technical Report LBNL-42584, Lawrence Berkeley National Laboratory, 1998.

[10] W P Segars, D S Lalush, and B M W Tsui. Modeling respiratory mechanics in the MCAT and spline-based MCAT phantoms. In J A Seibert, editor, *1999 IEEE Nuclear Science Symposium and Medical Imaging Conference Record*, pages 985–989, 2000.